

The Effect of Bridge Geometry on Microstructure and Texture Evolution During Porthole Die Extrusion of an Al–Mg–Si–Mn–Cr Alloy



YU WANG, ANDREW ZANG, YAHYA MAHMOODKHANI, MARY WELLS, WARREN POOLE, and NICK PARSON

Porthole die extrusion is used to produce complex hollow aluminum cross-sections for automotive applications. In a porthole die, the material is first divided into multiple streams which are separated by a bridge, before rejoining in the weld chamber and finally passing through the die orifice. The rejoining of the material in the weld chamber produces lines known as weld lines in the final extruded product. The microstructure along the weld line and its associated quality are strongly influenced by the thermal-mechanical history the material experiences as it passes through the portholes, the weld chamber, and the die orifice, which can be altered by die design and, in particular, the bridge geometry. To study the influence of bridge geometry on weld line microstructure and final quality, a series of porthole die extrusion experiments was conducted using an Al–Mg–Si–Mn–Cr alloy and two different types of bridge geometry (streamlined and flat). The experimental results showed that bridge geometry had a significant effect on the local microstructure and crystallographic texture at the weld line. Specifically, EBSD analysis indicated that the weld line texture associated with a streamlined bridge geometry consisted of a deformation texture (mainly the copper component), while the local texture produced by a flat bridge was a recrystallization texture consisting of Cube, Goss, and Cube_{RD} texture components. Simulation of the extrusion process, using DEFORM 3D, indicated that the weld line produced using a flat bridge experienced a slightly higher temperature, but much higher equivalent strains than the streamlined case. Material away from the weld line was very similar for both cases, indicating that the effect of the die bridge geometry is localized to the region close to the weld line.

<https://doi.org/10.1007/s11661-021-06322-5>

© The Minerals, Metals & Materials Society and ASM International 2021

I. INTRODUCTION

LIGHTWEIGHTING of vehicles is an important strategy to reduce fuel consumption and the associated green house gas emissions for internal combustion engine powered automotive vehicles. In addition, lightweighting is also viewed as an enabling technology to extend the range of battery or fuel cell powered vehicles. As a result, hollow aluminum profiles extruded using porthole dies are increasingly utilized in vehicles

such as the aluminum intensive Ford F-150.^[1] A porthole extrusion die is usually made up of two parts: a die mandrel and a die plate. The mandrel incorporates multiple portholes which are separated by structures known as bridges. During porthole extrusion, the bridges act to divide the billet into a number of separate metal streams that pass through the portholes. In the weld chamber, these metal streams rejoin to form a continuous shape. At each location where the metal streams rejoin, longitudinal weld lines are formed. Finally, the material is extruded through the orifice in the die plate producing the final desired profile shape.

It is important to understand the response of the weld line to plastic deformation during (i) forming of parts, e.g., hydroforming, (ii) joining of extrudates with self-piercing rivets and (iii) during crash of the vehicle.^[2,3] Many researchers have found that the shape and size of the bridge has a significant effect on the weld quality in the final extruded product.^[4–7] For example, Gagliardi *et al.* simulated porthole die extrusion using eight different die bridge geometries and found that a

YU WANG, YAHYA MAHMOODKHANI, and MARY WELLS are with the Mechanical and Mechatronics Engineering Department, University of Waterloo, 200 University Avenue West, Waterloo, ON N2L3G1, Canada Contact e-mail: y2275wan@uwaterloo.ca. ANDREW ZANG and WARREN POOLE are with the Department of Materials Engineering, The University of British Columbia, 309-6350 Stores Road, Vancouver, BC V6T1Z4, Canada. NICK PARSON is with the Rio Tinto Aluminum, Arvida Research and Development Center, Saguenay, QC G7S4L2, Canada.

Manuscript submitted December 18, 2020; accepted April 30, 2021.
Article published online May 19, 2021

rhombus shaped bridge created smoother metal flow and a higher pressure in the weld chamber compared to a flat bridge.^[6] As a result, a strip extruded using a rhomboidal bridge exhibited improved tensile ductility compared to a strip extruded using a flat bridge.^[8]

In recent years, researchers have used Finite Element (FE) models as a tool to quantitatively understand the connection between the thermomechanical history experienced by the material during porthole die extrusion, and the resulting microstructure and texture in the final extrudate.^[9–12] For example, Chen *et al.* calculated the volume fraction of dynamically recrystallized grains inside a porthole die cavity using the calculated strain and temperature obtained from a finite element method (FEM) simulation.^[11] Further, Tang *et al.* used the deformation history calculated from a FEM model as an input to a viscoplastic self-consistent (VPSC) polycrystal plasticity model to predict texture evolution during porthole die extrusion for a micro-tube produced using an AA1100 aluminum alloy.^[9]

Although some researchers have examined texture evolution during porthole die extrusion, these have been focused on one specific die configuration, *i.e.*, they have not considered the effect of different bridge geometries on the microstructure and texture of the final extruded product.^[13–15] In particular, it is of significant scientific and technical interest to examine how the details of the bridge geometry affect the local microstructure and crystallographic texture, since this will influence the local mechanical response. In this research, a series of extrusion trials were conducted using idealized die geometries to examine the influence of the bridge geometry (streamlined and flat). Specifically, the die was designed with the portholes offset from the billet center, *i.e.*, similar to the situation for one face of a square or rectangular porthole tube extrudate. These experiments were complemented by FEM simulations of the porthole die extrusion process so that the metal flow and thermal-mechanical history could be analyzed for the two bridge geometries and linked to the final microstructure and texture of the extruded strip. The results were then used to rationalize the microstructures and textures found along the weld line for the different bridge die geometries.

II. EXPERIMENTAL

A. Extrusion Trials

The material used in this research was an Al–Mg–Si–Mn–Cr alloy, with the composition shown in Table I (note: the composition falls in the range of AA6082). Extrusion billets with a diameter of 101.6 mm and a

length of 400 mm were direct chill (DC) cast at Rio Tinto Aluminum’s Research and Development Laboratory in Saguenay, Quebec, Canada. The average grain size of the as-cast billets was determined to be 120 μm and its crystallographic texture was nearly random.^[16] After casting, the billets were homogenized by heating to 500 $^{\circ}\text{C}$ at a rate of 250 $^{\circ}\text{C}/\text{h}$ followed by heating at 50 $^{\circ}\text{C}/\text{h}$ to 550 $^{\circ}\text{C}$ where the billet was held for 2 hours and then water quenched. The mean radius of Mn/Cr containing dispersoids was measured by Liu *et al.* to be 37 nm with a volume fraction of 1.3 pct.^[16]

After homogenization, the billets were extruded with an instrumented extrusion press using porthole dies with two different bridge geometries. Figure 1 shows a schematic diagram of the porthole die assembly and Figure 2 provides a cross-section through the die showing the details of the streamlined and flat bridge geometries. The extrudate was designed to have dimensions of 50 \times 2.5 mm with a weld line running longitudinally down the middle. The height of the weld chamber was 12.7 mm and the width of the bridge was 8 mm. As shown in Figure 1(d), the portholes were located slightly offset from the center line of the die so that the metal flow would be similar to the case for one face of hollow profile. The design of the die bearing is important to balance the material flow at the die exit and prevent distortion of the extrudate.^[17] Due to the friction caused by the bridge and die walls, the exit velocity of the material at the edge and center of the extrudate can be slower if the bearing length is uniform. As a result, the bearing length at the edge and the center is shorter (see Figure 1(e)) in order to lower friction from the die bearing at these positions, thus, improving the uniformity of exit velocity profile across the cross-section of the extrudate.

The extrusion trials were conducted at an initial billet temperature of 480 $^{\circ}\text{C}$ (induction heated to this temperature at 250 $^{\circ}\text{C}/\text{min}$) using a ram speed of 5 mm/s. For each trial, two initial billets were extruded to warm up the die and then another four billets were run consecutively. The die and container temperatures were 450 $^{\circ}\text{C}$. The profiles were quenched using a standing wave water tank located 2.5 m from the die exit.

B. Characterization

The microstructure and crystallographic texture of the extrudates were characterized using optical microscopy and electron backscatter diffraction (EBSD). The samples were prepared by grinding with silicon carbide papers and final polishing with 1 μm diamond particles. For the optical microscope observations, the polished samples were anodized using Barker’s reagent, a mixture of 6 ml (48 pct) HBF_4 and 200 ml distilled water with a voltage of 30 V for \approx 60 seconds. For EBSD, the samples were given an additional polish using 0.05 μm colloidal silica, and then cleaned with ethanol in an ultrasonic bath for 5 minutes. EBSD measurements were conducted using a Zeiss-Sigma SEM equipped with a Nikon high-speed camera. The EBSD tests were performed using the following parameters: accelerating

Table I. Composition of the Alloy Used in Extrusion Trials (Wt Pct)

Alloy	Mg	Si	Mn	Cr	Fe	Al
Al–Mg–Si–Mn–Cr	0.70	1.04	0.5	0.15	0.20	balance

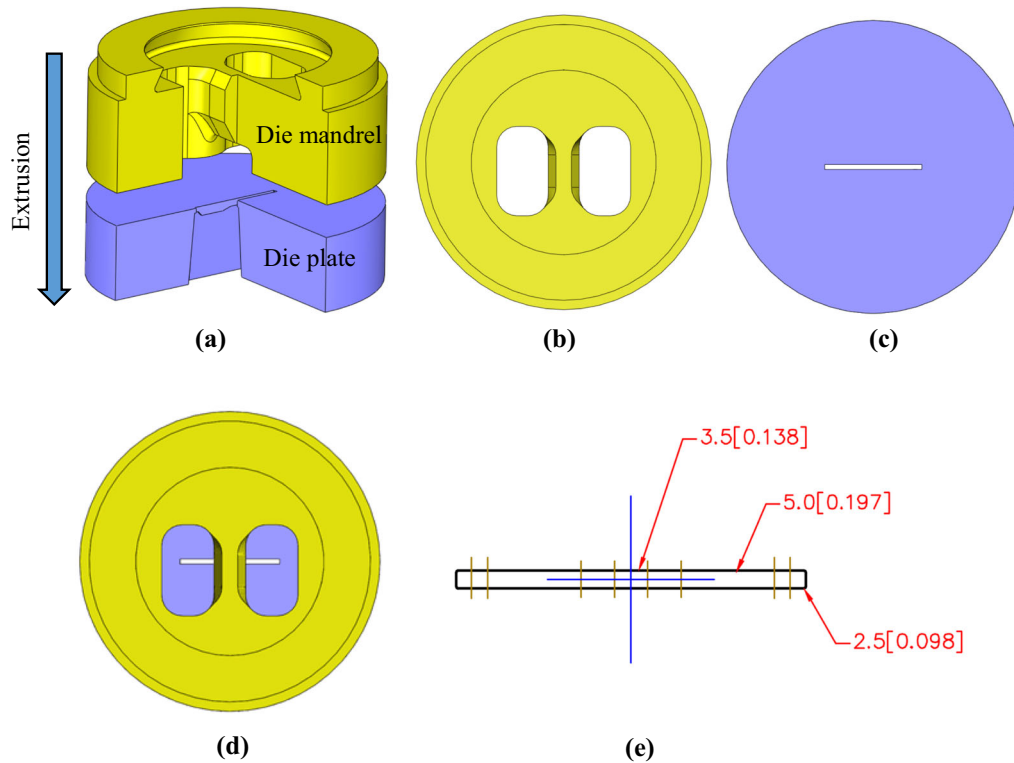


Fig. 1—CAD drawings showing the (a) split porthole die assembly, (b) top view of the die mandrel, (c) top view of the die plate, (d) view through the portholes showing the position of die exit orifice, and (e) details on the bearing length of the extrusion die.

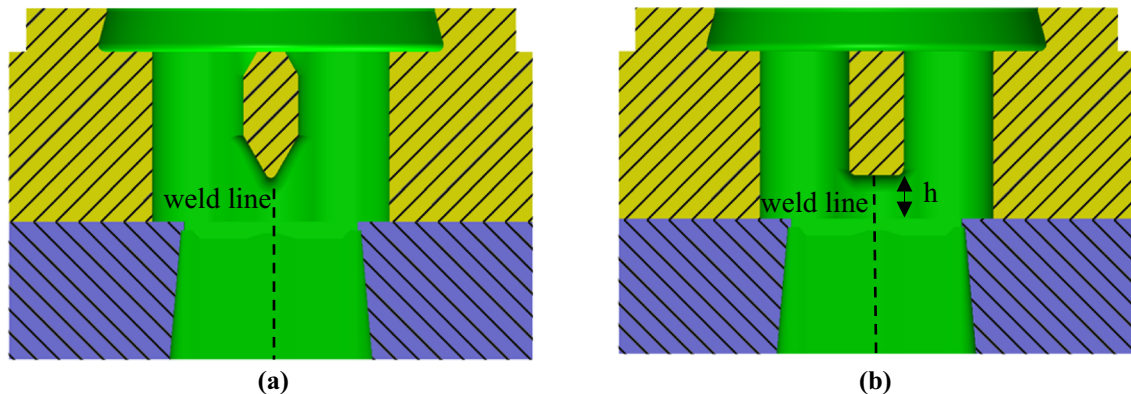


Fig. 2—A schematic showing the cross-section of the die for the two bridge geometries: (a) streamlined bridge and (b) flat bridge. The height (h) of the welding chamber was 12.7 mm (and width of bridge was 8 mm). Note: the green region in the schematic represents the inside of the empty die (Color figure online).

voltage of 20 kV, working distance of 13 mm and a step size of 200 nm. The EDAX/TSL-OIM Analysis software (8th edition) was used to process the data. The EBSD maps were cleaned using a grain dilation method where the orientation of measurements of less than five pixels was re-orientated to its neighboring grains.

C. Finite Element Method Model

The porthole die extrusion process was modeled using the ALE (Arbitrary Lagrangian Eulerian) module in the commercial finite element (FE) code DEFORM 3D. In the ALE simulation, the mesh nodes are neither

connected to the material, nor fixed in the space, but move independently from the material.^[18] Unlike Lagrangian simulations, the movement of the mesh nodes with respect to the material domain alleviates the mesh distortion and the need for re-meshing associated with large plastic strains. As a result, the ALE simulation has the advantage of being able to simulate extrusion processes efficiently, capturing the state variables, flow paths, and thermo-mechanical history. Despite the advantages of the ALE approach, it can only capture a snapshot, showing the load and state variables at steady state, *i.e.*, it is not able to simulate the entire extrusion process from breakthrough to

completion; the ram is stationary and does not move during the simulation. As a result, the ALE simulation model only describes the state of the extrusion at a specific ram position.

As shown by the dashed line in Figure 2, there is a symmetry plane which runs down the center of the process coinciding with the welding plane, and thus, only half of the billet and die need be considered, thereby reducing the simulation time. Figure 3 shows that all components including the container, ram, billet, and die were meshed using tetrahedral elements. In order to increase the efficiency of the simulation while not sacrificing accuracy, several mesh windows were applied to vary the element size spatially. For example, the smallest element size (0.2 mm) was used close to the die bearing as this area would experience a high gradient of stress and strain.

In order to maintain the welding interface free of contaminants, no lubricant was used during extrusion. Thus, the billet surface was assumed to stick to the tooling except at the die bearing.^[19,20] The friction between the billet and the tooling was described using a shear friction model with complete sticking condition^[21] at all locations except the die bearing, where a shear friction of 0.7 was applied.^[22] The heat transfer coefficient between the billet and the tooling was assumed to be $25 \text{ kW m}^{-2} \text{ K}^{-1}$ and the tool material was H-13 steel.^[23] The extrusion conditions were set to match those used during the extrusion trials, *i.e.*, the initial billet temperature was $480 \text{ }^\circ\text{C}$, the die and container temperatures were $450 \text{ }^\circ\text{C}$, and the ram velocity was 5 mm/s . The simulation parameters used in this research are summarized in Table II.

Considering aluminum alloys have a relatively high stacking fault energy, dislocation cross slip is easy, and as such dynamic recovery counters strain hardening during deformation. Thus, the flow stress of aluminum alloys typically reaches a steady-state regime at low strains (< 0.1) and remains independent of strain at high temperature.^[16,24,25] Based on this, the Sellars–Tegart model was used to describe the relationship between steady-state flow stress, strain rate and temperature,^[26,27] *i.e.*,

$$A[\sinh(\alpha\sigma)]^n = \dot{\epsilon} \exp\left(\frac{Q_d}{RT}\right) \quad [1]$$

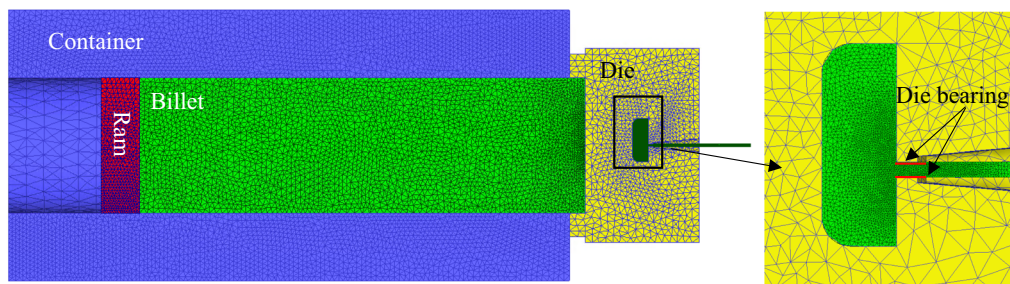


Fig. 3—A cross-section of the FEM model illustrating the mesh used for the simulation with an expanded view of the die bearing region shown to the right.

where σ is the steady-state flow stress (MPa), $\dot{\epsilon}$ is the strain rate (s^{-1}) and T is the temperature (K). A , α , n and Q_d are material constants and R is the universal gas constant ($8.314 \text{ J mol}^{-1} \text{ K}$). The material constants used in the Sellars–Tegart model can be determined using experimentally measured stress–strain curves at high temperature, and its effectiveness has been verified by many researchers working on hot forming of aluminum alloys.^[28–31] In this research, these material constants were determined by a fit of Eq. (1) to the flow stress data for AA6082 available in the DEFORM v10.0 database. Table III summarizes the values used in the current work.

Figure 4 shows an example of the flow path from the ALE simulation results. The DEFORM ALE simulation can provide the velocity field of the workpiece directly and from this the flow path is calculated. In this study, the flow paths were tracked backwards from the final extrudate through to the original undeformed billet. As shown in Figure 4, the coordinate of point a_i on the flow path is presumed to be determined by previous iterations, and the coordinate of a_{i+1} is to be determined in this step. The velocity of the tracked particle traveling from the point a_i to a_{i+1} is assumed to be the velocity of a_i point, v_i , so the coordinate of a_{i+1} is determined as

$$\vec{a}_{i+1} = \vec{a}_i - \frac{\vec{v}_i}{|v_i|} \times dl \quad [2]$$

where dl is the displacement between two consecutive points. The time, t_{i+1} for point a_{i+1} is determined as:

$$t_{i+1} = t_i - \frac{dl}{(|v_i| + |v_{i+1}|)/2} \quad [3]$$

which means that a time of t_{i+1} is needed for the back tracked point to flow from the position a_{i+1} to the original point a_0 . If the displacement increment dl is small, the flow path can be calculated accurately (in this case using a script written in MATLAB) as verified by Mahmoodkhani *et al.* for the problem of the transverse weld formation during billet on billet extrusion.^[33]

Table II. Simulation Parameters and Boundary Conditions Used in the DEFORM Model

Parameter	Value
Friction Between Tooling and Billet	sticking
Friction Factor on Die Bearing	0.7
Heat Transfer Coefficient	25 kW m ⁻² K ⁻¹
Ram Speed	5 mm/s
Initial Billet Temperature	480 °C
Initial Die Temperature	450 °C
Initial Container Temperature	450 °C
Tool Material	H-13 steel
AA6082 Heat Capacity	900 J/(kg K)
AA6082 Thermal Conductivity	180.2 W/(m K)
H-13 Heat Capacity at 500 °C to 600 °C	610 J/(kg K)
H-13 Thermal Conductivity	24.6 W/(m K)

Table III. Material Constants Used in Eq. [1] to Describe Constitutive Behavior for AA6082^[32]

Material Parameter	Value
A	$9.04 \times 10^8 \text{ s}^{-1}$
α	0.03 MPa^{-1}
n	5.0
Q_d	$145 \text{ kJ mol}^{-1} \text{ K}^{-1}$
R	$8.314 \text{ J mol}^{-1} \text{ K}$

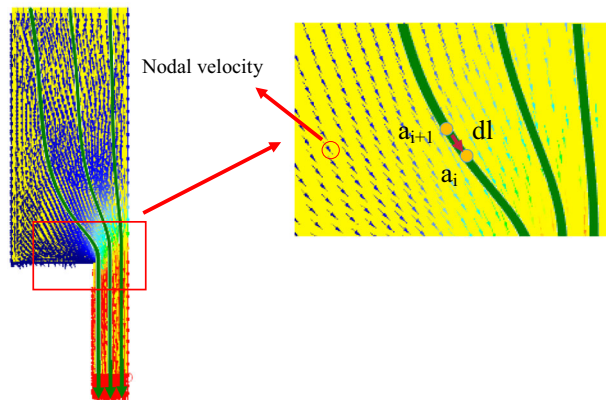


Fig. 4—Schematic drawing of point tracking based on ALE simulation.

Finally, it is noted that the ALE simulations are for the scenario of billet on billet extrusion and the force measured is at the beginning of the extrusion push, which corresponds to the loads measured in the experiments.

D. Model Assessment

In order to assess the accuracy of the simulations, the model predictions for the load were compared to the experimental measurements from the extrusion trials. The breakthrough loads measured during the experiments for the streamlined and flat bridges were 701 and

707 tons, respectively, which compares with the ALE predictions of 692 and 703 tons, *i.e.*, a difference of ≈ 1 pct. Further, both experimental and simulation results showed that the flat bridge required a slightly higher extrusion load than the streamlined bridge. Gagliardi *et al.* suggested that the effect of the bridge on extrusion load was determined by the volume and shape of the bridge.^[6] In this research, the volumes of the streamlined and flat bridges were 1.7×10^4 and $2.0 \times 10^4 \text{ mm}^3$, respectively. Since the flat bridge had a larger volume and more irregular surface compared to the streamlined bridge, the results are consistent with the extrusion load being slightly higher for the flat bridge.

The predictive capability of the simulation was also verified by comparing the location and thickness of the dead metal zones (DMZ) between simulation and experiment. For the experiment, a slice was sectioned from material which had been extracted from a die removed and immediately quenched at the end of extrusion. Figure 5(a) shows the position of the section for the in-die material, *i.e.*, it is a plane perpendicular to the extrusion axis taken 6.35 mm away from the tip of the streamlined bridge. Figure 5(b) shows that the material in the dead zones etches to a different contrast and this region has been delineated with dashed black lines. It can be observed that there are DMZs at the four corners, and the area of the DMZ closer to the die orifice was smaller than the DMZ farther away due to the asymmetric geometry of the portholes. In the model simulation, the DMZ was defined as the region where the velocity was below 0.3 mm/s, and is highlighted light blue in Figure 5(c). The model-predicted DMZ is similar to the DMZ shown in the sliced plane providing confidence that the model was able to simulate the material flow.

III. RESULTS AND DISCUSSION

A. Metallography of Extruded Samples

Figure 6 shows that the grain structures near the weld line (as revealed by Barkers etch) consisted of peripheral coarse grains (PCG) at the surface and fine grains in the center. The PCG layer was quite uniform in thickness ($\approx 100 \mu\text{m}$) in the material on either side of the weld line and independent of the bridge geometry. A roughly triangle shaped region of larger recrystallized grains can be observed at the surface near the weld line. The grain structure on the weld line away from the surface was very fine without obvious coarsening, even considering the very high extrusion temperature. It is assumed that the presence of a high density of Mn/Cr dispersoids pinned the movement of the boundaries, making recrystallization and grain growth limited.^[34,35]

B. Crystallographic Texture of the Extruded Samples

Two regions near the mid-thickness of the extruded strips were investigated using EBSD to measure the local grain structure and crystallographic texture as

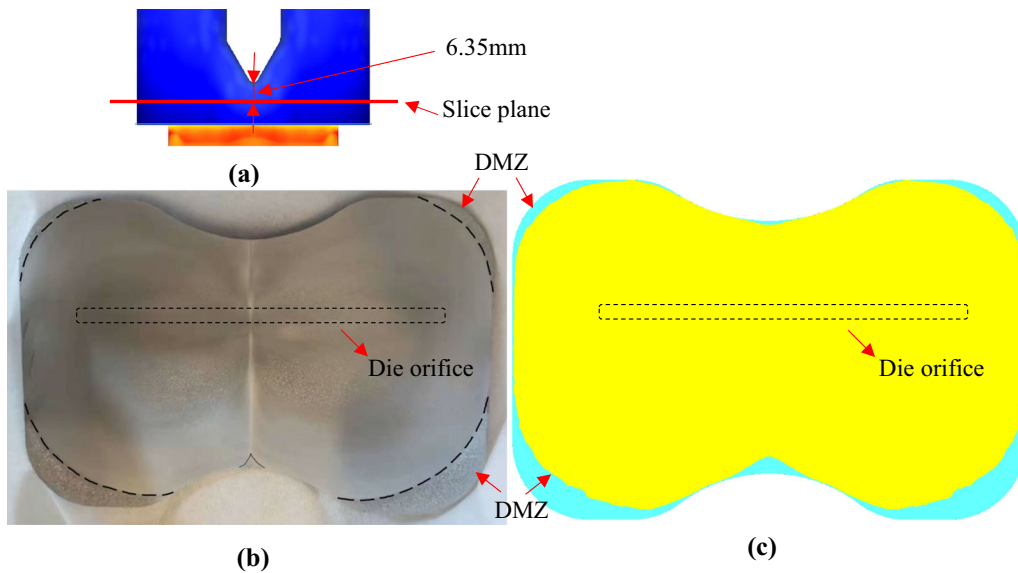


Fig. 5—Comparison between the experimental and model-predicted DMZ locations for the streamlined bridge extrusion case: (a) plane location, (b) experimental result, and (c) model prediction.

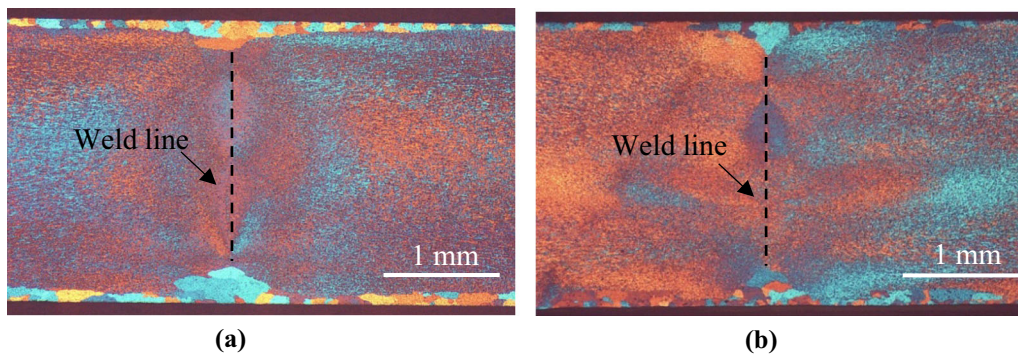


Fig. 6—Optical microscope image (under polarized light) of the cross-section of the strip illustrating the weld line of profiles extruded using (a) a streamlined bridge and (b) a flat bridge.



Fig. 7—Regions on the extruded strip studied by EBSD.

shown in Figure 7, *i.e.*, the weld line and the quarter width regions.

Starting with the midpoint region at the quarter width position, Figure 8 shows an EBSD map where the grains have been colored by their ideal texture components. The grains had a pancaked shape due to the much higher compressive strain in the thickness direction relative to the width direction. The microstructures associated with the two bridge geometries had comparable grain morphologies and crystallographic orientations. In more detail, Figure 9 shows the 001 and 111 pole figures for the two cases and it can be observed that the crystallographic texture was similar showing that there was no effect of the bridge geometry at the quarter width position. As the deformation conditions were

close to plane strain in this region, the texture can be quantified in terms of the ideal deformation texture components (copper, brass and S) and recrystallization texture components (Cube, Goss and $Cube_{RD}$) as summarized in Table IV. For both the streamlined and flat bridges, the texture consisted of copper (≈ 10 to 11 pct), brass (≈ 26 to 30 pct) and S (≈ 48 to 53 pct) components with only a small fraction (less than 4 pct) of Goss, Cube or $Cube_{RD}$ oriented grains, *i.e.*, the orientations associated with recrystallization. In summary, for both cases, approximately 90 pct of the grains were oriented near the ideal deformation texture components, and thus it is summarized that this region is primarily unrecrystallized regardless of the bridge geometry.

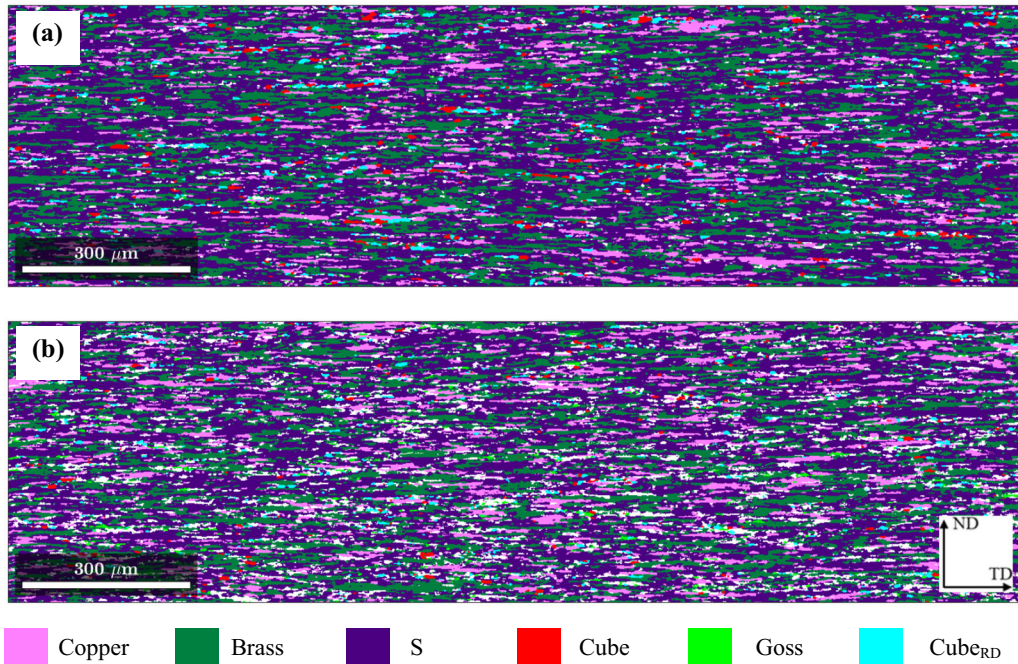


Fig. 8—Spatial distribution of ideal texture components for the quarter width region of strips near the midpoint: (a) streamlined bridge and (b) flat bridge. Note: for each texture component, the color represents those grains within 15 deg of ideal component. White areas represent other orientations (Color figure online).

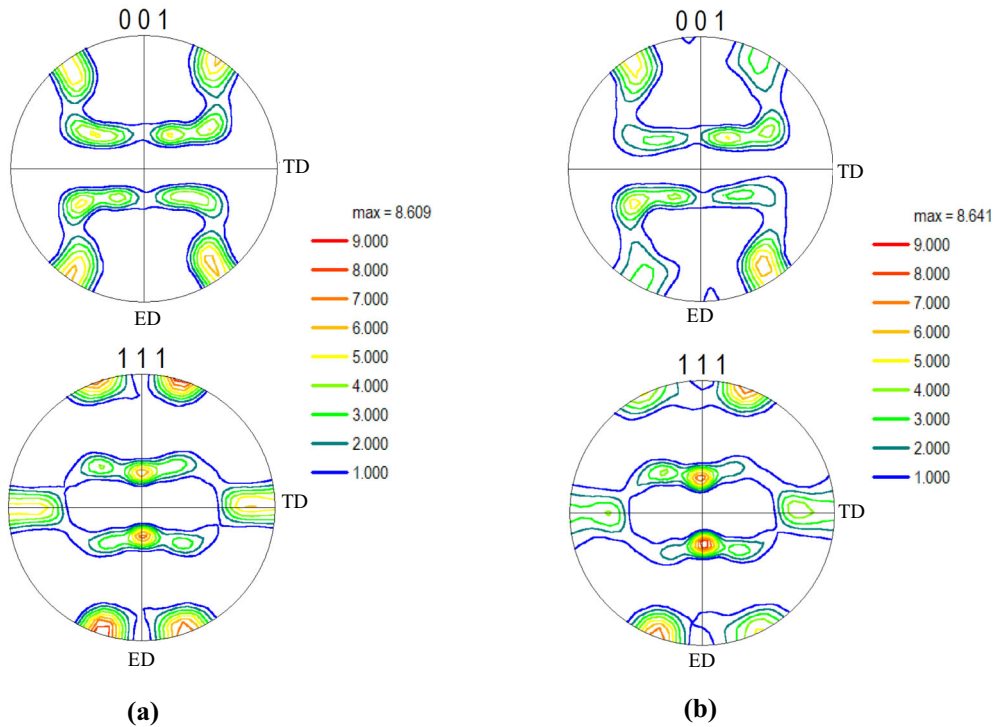


Fig. 9—Pole figures of quarter width region of strips: (a) streamlined bridge and (b) flat bridge. Note: pole figures were assessed from ≈ 6000 grains.

Figure 10 shows EBSD maps colored by the ideal deformation and recrystallization texture components for the weld line region from the samples with streamlined and flat bridges. Starting with the streamlined

bridge (Figure 10(a)), the average grain equivalent area diameter grain size was measured to be $10 \mu\text{m}$. In terms of crystallographic texture, one observes that there is a region of $\approx \pm 200 \mu\text{m}$ around the weld line where the

grain orientations are dominated by orientations near the Copper (pink) and S (purple) texture components with a small amount of Cube (red) and Cube_{RD} (light blue). To either side of this region, the texture evolves with evidence for grains with a Brass (green) orientation. Figure 11(a) shows 001 and 111 pole figures for the entire region in Figure 10(a) and Table V summarizes the volume fraction of the various ideal texture components (with 15 deg of ideal). From the pole figures and Table V, it can be seen that the major texture components in this region are the Copper (47.4 pct) and lesser amounts of S (23.1 pct) and Brass (6.9 pct), *i.e.*, the total fraction of the deformation texture components is 77.4 pct. Only ≈ 11 pct of the grains fall within the orientation for the ideal texture components associated with recrystallization (Cube, Goss and Cube_{RD}).

Chen *et al.* have proposed that the fine grain structure formed near the weld line may be due to geometric dynamic recrystallization (GDRX) occurring near the surface of the bridge due to the high strain and temperatures,^[13] where it is noted that the GDRX texture would be expected to be similar to the deformation texture. In terms of the observed textures, Tang *et al.* observed that a strong simple shear deformation texture formed at the surface of the bridge during extrusion.^[9] It is proposed that the strong simple shear texture associated with material entering the weld chamber would evolve toward a plane strain deformation texture. However, since the incoming texture close to the bridge has a strong simple shear texture, it evolves preferentially to a specific component of the usual plane strain texture, *i.e.*, the copper component. This is in contrast to the situation near the quarter width since the incoming material from the porthole will now have a different texture than the near bridge surface (due to a lower level of simple shear as one moves further from the direct contact with the bridge). The nearly plane strain deformation in the weld chamber then causes the texture to evolve toward the more conventional plane strain texture as shown in Figure 9 and summarized in Table IV, *i.e.*, with a much lower fraction of the Cu component and higher fractions of Brass and S components than observed for the material near the weld line.

Turning to the case of the flat bridge, Figure 10(b) shows an EBSD map displaying the spatial distribution of ideal texture components at the welding region for the sample extruded using the flat bridge. The average grain diameter was measured to be $8.5 \mu\text{m}$ which is similar to the measurement from the streamlined die. On the other hand, the textures were different with the flat bridge sample having significant volume fractions of Cube (red), Goss (bright green) and Cube_{RD} (light blue) recrystallization components (a total of 55 pct) and low fractions of Copper, Brass and S deformation components (17.3 pct). Yu *et al.* ascribed the formation of Cube and Goss texture components to possible dynamic recrystallization in the welding chamber.^[10] Further, Fan *et al.* proposed that the high level of deformation when metal streams come together in the weld chamber can prompt recovery and recrystallization of the material.^[36] This would be consistent with the observation of Wang *et al.* that the cube texture was also found in the

interface layer of AA3003 aluminum alloy after accumulative hot roll bonding, *i.e.*, a region of very high local strain.^[37]

In summary, it is proposed that based on crystallographic texture observations, the weld zone microstructure at the midplane of the streamlined die is primarily unrecrystallized and the microstructure for the same region from the flat die is primarily recrystallized.

IV. MODEL RESULTS AND DISCUSSION

A. Exit Temperature

Figure 12 presents the predictions from the FEM for the spatial distribution of temperature at the die exit from the ALE simulation for the two cases. It can be observed that the model predicts a higher exit temperature near the weld line for the die with a flat bridge, compared to the streamlined bridge. Figure 13 shows in more detail the temperature along the welding at the die exit (black dotted line in Figure 12(b)) for the bridge geometries, and it can be observed that the temperature predictions for the flat bridge are $\approx 4 \text{ }^\circ\text{C}$ higher than for the streamlined bridge.

B. Flow Path

The FEM model was used to quantify the effect of bridge geometry on the material flow as it passes through the die. This analysis was conducted by tracing the flow history of two points on the extruded strip cross-section for the two bridge types. The two points were chosen to represent mid-thickness locations at the weld line and at a quarter width location away from the weld line, *i.e.*, similar locations to where the EBSD measurements were done.

Figure 14 shows a contour map illustrating the magnitude of the local material velocity for the mid-thickness plane. The streamline of the flow path is shown in black for the center of the extrudate and in green for the quarter width location. It can be seen that the streamlines at the center depend on the bridge geometry, while the quarter width streamlines do not, *i.e.*, the flow path is similar for both bridge cases. Further, the time needed for each tracked point to flow around the bridge and pass through the welding chamber was also calculated and labeled beside the streamline. Here, it is important to note that there is a significantly longer time needed in the case of the die with a flat bridge. In order to rationalize the reason for the significantly different times for the material to flow around the different bridge geometries, it is useful to examine details of the local velocity field. It can be seen that in the case of the die with a flat bridge, there was a DMZ on the exit side of the bridge (marked with the black rectangle in Figure 14(b)), while no DMZ was seen for streamlined bridge at this location. The DMZ is essentially a rigid zone where the material velocity is close to zero. As a result, in the case of the die with a flat bridge, the streamline of center point entered the DMZ where the velocity was low thereby increasing the time

Table IV. Fractions of Ideal Texture Components at the Midplane of the Quarter Width Position Based on EBSD Measurements (the Fractions Were Calculated Based on the Intensities Within 15 deg of the Ideal Plane Strain Deformation Textures)

Die Configurations	Copper (Pct)	Brass (Pct)	S (Pct)	Cube (Pct)	Goss (Pct)	Cube _{RD} (Pct)
Streamlined Bridge	10.7	30.3	52.7	1.5	0.2	2.2
Flat Bridge	11.3	26.7	48.5	0.6	1.0	1.4

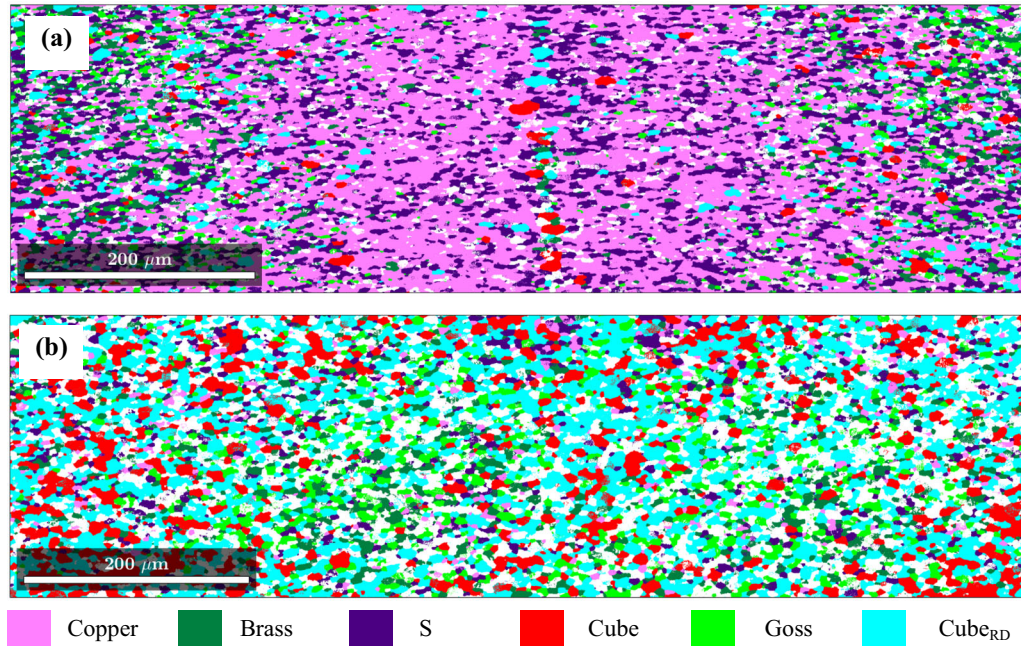


Fig. 10—Spatial distribution of texture components at welding region: (a) streamlined bridge and (b) flat bridge. Note: for each texture components, the color represents those grains within 15 deg of ideal component. White areas represent other orientations (Color figure online).

for this material to flow through the die. The model-predicted flow path calculations indicated that it took about 4.9 seconds for the tracked center point to flow around the streamlined bridge and pass through the welding chamber, while it took about 11 seconds for the tracked center point to flow through the same region using the flat bridge (it should be noted that this difference depends strongly on the exact position of the streamline relative to the bridge surface). On the other hand, the presence of the bridge had essentially no effect on the streamlines at the quarter width position and the time to pass through the die was 1.4 seconds for both cases.

C. Strain Distribution

The accumulated plastic strain was calculated by integration of the effective strain rate over time along the flow path, as shown in Eq. 4.

$$\varepsilon = \int \dot{\varepsilon}_{\text{effective}} dt \quad [4]$$

Figure 15 illustrates the results for the predicted strain distribution (von Mises equivalent strain) in the

cross-section of the extruded profiles for the two different bridge geometries. The strain was high at the surface of the extrusion (particularly at the corners) and at the weld line. In the case of the die with a streamlined bridge, the high strain region at the weld line was lenticular shaped, aligned on the weld line with a maximum width of ≈ 1 mm. In contrast, the corresponding region for the die with a flat bridge was cross shaped with a maximum width of ≈ 2.5 mm. It is noted that this is consistent with the EBSD measurements shown in Figure 10, where it can be observed that the width of the zone with a modified texture was approximately twice as large for the die with flat bridge compared to the die with a streamlined bridge. Another observation worth noting is that the strain distribution on the weld line was slightly asymmetric. This is related to design of the die where the portholes were offset from the center as shown in (Figure 1(b)). Figure 16 shows the strain distribution along the mid-thickness of the profile from the weld line to the edge. At the weld line, the material extruded with the flat bridge exhibited ≈ 50 pct higher equivalent strain but the strain decreased rapidly further away from the weld line. At a position of ≈ 5 mm from the weld line, the strains associated with the two bridge geometries are essentially the same.

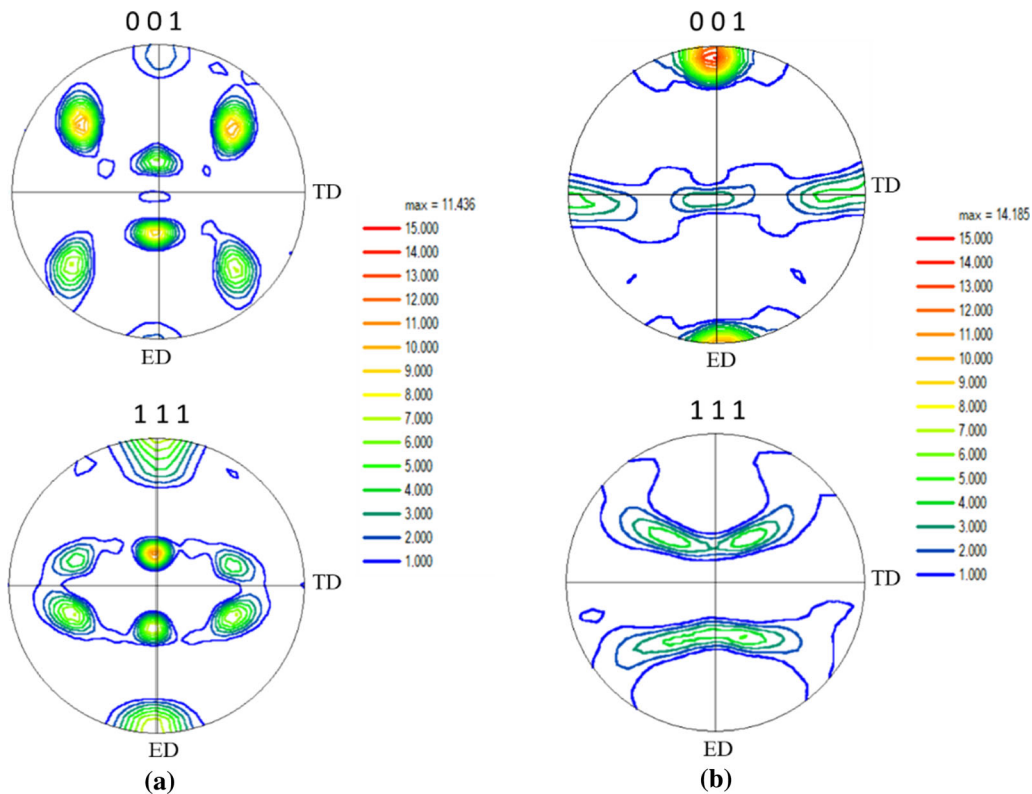


Fig. 11—Pole figures for region near weldline: (a) streamlined bridge and (b) flat bridge. Note: pole figures were assessed from ≈ 6000 grains.

Table V. Fractions of Texture Components at the Weld Line Region Based on EBSD Measurements (the Fractions Were Calculated Based on the Intensities Within 15 deg of the Ideal Plane Strain Deformation Textures)

Die Configurations	Copper (Pct)	Brass (Pct)	S (Pct)	Cube (Pct)	Goss (Pct)	Cube _{RD} (Pct)
Streamlined Bridge	47.4	6.9	23.1	2.2	3.9	5.0
Flat Bridge	3.1	7.9	6.3	15.9	8.6	30.5

Figure 17 shows the FEM model predictions for the effective strain rate distribution taken from a cross-section cut along the middle thickness plane. By tracking selected streamlines (green line for the quarter width and black for the center) and integrating the effective strain rate, the strain history of the streamlines was calculated for both bridge geometries as shown in Figures 18 and 19. The history along a porthole die extrusion streamline can be divided into four stages: splitting of the flow into two parts, flowing through the portholes, rejoining of the flow in the weld chamber and exit through the die orifice^[38] (Figure 17). In the splitting stage, the billet was split into two metal streams and squeezed into the portholes. A substantial amount of deformation occurred during the splitting stage and the strain accumulated during splitting was affected by the bridge geometry. Referring to Figure 18, the magnitude of the equivalent strain for the center point in dies with streamlined and flat bridges as it enters the portholes was ≈ 6 and ≈ 9 , respectively. The blunt surface of the flat bridge made the splitting of the billet more difficult

and thus accumulated a higher strain as the material entered the porthole. Inside the portholes, the center point had to flow very close to the bridge surface, where the strain rate was extremely high due to friction between the material and the bridge wall (Figure 17), so the equivalent strain value increased sharply. In the case of the die with the flat bridge, the equivalent strain increased from ≈ 9 to ≈ 53 as the material passed through the porthole. On the other hand, the equivalent strain increased from ≈ 6 to ≈ 40 for the case of the streamlined die, reflecting the shorter length of the bridge which is parallel to the extrusion direction. It is also worth noting that the material traced back from the weld line had a much sharper turn after coming off the bridge for the case of the die with the flat bridge (see Figure 14), and thus a higher strain was accumulated in the weld chamber compared to the die with streamlined bridge extrusion, *i.e.*, as shown in Figure 18. This accumulated strain is almost 3 times larger than for the die with a flat bridge. On the other hand, Figure 19 shows that at the quarter width point, the material in the

porthole which was far away from the surface of the bridge was uninfluenced by the bridge design. As a result, the material traced back from the quarter width exit experienced only accumulated a relatively small amount of equivalent strain as it entered and passed through the porthole, *i.e.*, approximately a strain of ≈ 1 . In the final step, the material from all streamlines entered the weld chamber and reached the maximum

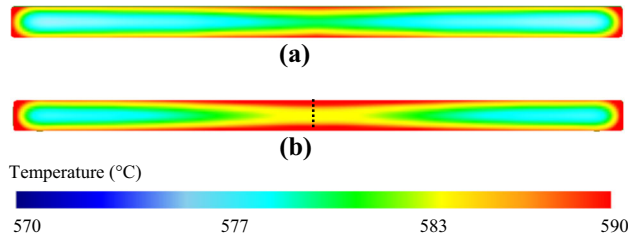


Fig. 12—Model-predicted temperature distribution throughout the cross-section of the extruded profile at the die exit: (a) die with a streamlined bridge and (b) die with a flat bridge.

equivalent strain value as it was forced through the die

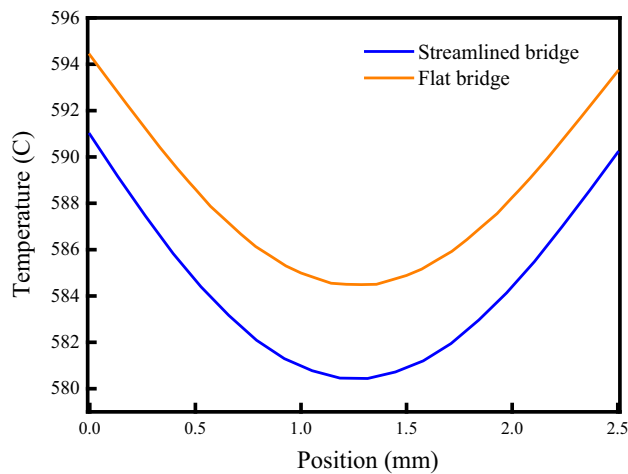


Fig. 13—Temperature distribution along the weld line at the die exit for two bridge geometries extrusion.

orifice. Additionally, it is of interest to compare the total equivalent strain with that of the ideal deformation. The ideal equivalent strain is 4.2, (*i.e.*, $\epsilon_{ideal} = \ln\left(\frac{A_o}{A_f}\right)$ where A_o and A_f are the cross-sectional area of the initial and final sample, respectively, and this compares with the total equivalent strain of 5.7 for the quarter width streamline (see Figure 19). The difference here primarily arises from the aforementioned redundant strain associated with the material passing through one of the portholes. In contrast, the total equivalent strain for the material near the weld line is ≈ 42 and ≈ 62 for the dies with streamlined and flat bridges, respectively, which is 10 to 15 times greater than the ideal deformation.

Returning to the spatial differences in the microstructure and crystallographic texture shown in Figures 8 and 10 for the quarter width and weld line regions, it is worth summarizing the relationship to the FEM modeling results. First, at the quarter width, it is clear that the strain history does not depend on the geometry of the bridge, as shown in Figure 19, and this is consistent with the observation that the grain shape and crystallographic texture was essentially the same for both dies (see Figure 8). On the other hand, the difference between the microstructure observed for the region near the weld line, *i.e.*, primarily unrecrystallized for the die with the streamlined bridge and recrystallized for the flat bridge die, can be rationalized by the effect of the bridge shape on the local thermal-mechanical history. First, it is noted that the die exit temperature is higher in the case of the flat die, but only by a small amount, ≈ 4 °C, and as such, probably does not account for the difference. However, the evolution of strain for the material traveling along this streamline is very different, as seen in Figures 16, 17, and 18. The higher level of accumulated equivalent strain (42 vs 62 for streamline and flat bridges, respectively) suggest an increased propensity for recrystallization in the die with the flat bridge, consistent with experimental observations in Figure 10. The details of the recrystallization mechanism under these conditions (very high total strain and high strain rates) remain challenging to verify experimentally, *i.e.*, GDRX, continuous dynamic recrystallization or static recrystallization after the sample leaves the die. However, Mahmoodkhani *et al.* have recently proposed that it is

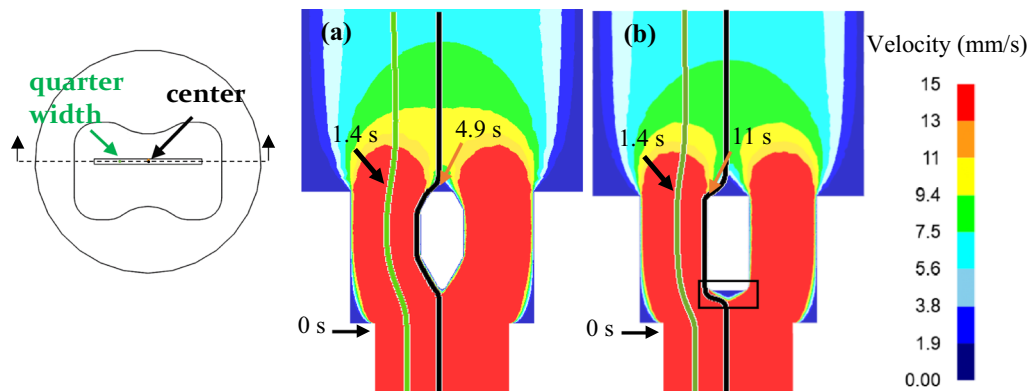


Fig. 14—FEM model-predicted velocity field map for (a) the die with a streamlined bridge and (b) the die with a flat bridge.

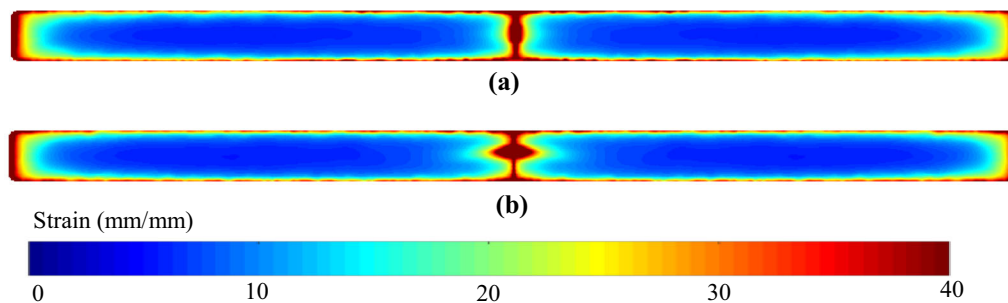


Fig. 15—Effect of bridge design on the distribution of von Mises equivalent strain distribution for (a) the die with a streamlined bridge and (b) the die with a flat bridge.

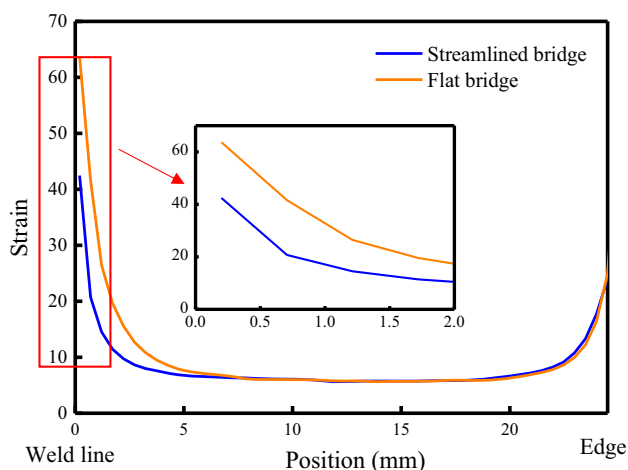


Fig. 16—FEM model predictions for the von Mises equivalent strain profile plotted at the mid-thickness of the extruded strip going from the weld line to the edge for dies with flat and streamlined bridges.

the local stored energy which correlates with recrystallization.^[32] This would be consistent with the current results and is of interest for future detailed simulation studies.

Finally, it is worth commenting on the difference in local crystallographic texture for the streamlined die, *i.e.*, the case where minimal recrystallization occurred. The quarter width and center regions both exhibited components of ideal plane strain deformation textures associated with the final material flow through the die orifice which occurs under nearly plane strain conditions. However, the relative fractions of the Copper, Brass and S components were significantly different with, for example, the Copper component being ≈ 5 times higher for the weld line region compared to the quarter width. It is proposed that this difference can be rationalized by the different strain histories of the material on the different streamlines. The accumulated strain prior to passing through the die orifice can be estimated by taking the difference between the ideal deformation and the total strain calculated from the FEM model, in this case a strain of 1.5 and 38 for the quarter width and weld line streamlines. It is proposed that the very large strain and the nature of the local strain path (predominately simple shear due to friction between the bridge and the material flowing past it)

prior to the final stage of passing through the die orifice influences the relative fractions of the deformation texture components selected. It would be of interest to examine this hypothesis in the future using crystal plasticity simulations.

V. SUMMARY

In this research, the effect of porthole die bridge geometry on microstructure and crystallographic texture was experimentally investigated for an Al–Mg–Si–Mn–Cr (in the family of AA6082). The extrusion process was also simulated using DEFORM 3D to obtain the thermal-mechanical history for the different bridge geometries. The simulations were able to rationalize the differences in microstructure and texture produced using dies with streamlined and flat bridges. The main outcomes of this work can be summarized as follows:

1. The crystallographic texture and microstructure for material near the weld line are influenced by bridge geometry. The crystallographic texture produced by a streamlined bridge near the weld line and had a strong Copper component (typical of a plane strain deformation texture), whereas the flat bridge resulted in Cube, Goss, and Cube_{RD} texture components consistent with the microstructure having a predominate recrystallization texture.
2. The bridge geometry has a significant effect on material flow behavior and thermal-mechanical history during porthole die extrusion. The simulation predicted higher accumulated equivalent strains for a streamline corresponding to the weld line for the die with a flat bridge and a slightly higher local temperature compared to the die with a streamlined bridge. The observation of a recrystallization texture for the case of the flat bridge was rationalized based on the significantly higher equivalent strain and local strain rate experienced by this material as it passes through the die.
3. The effect of the bridge design was localized to a region around the weld line. At the quarter width position, the thermomechanical history was similar for the two bridge designs resulting in similar microstructures and crystallographic textures. The

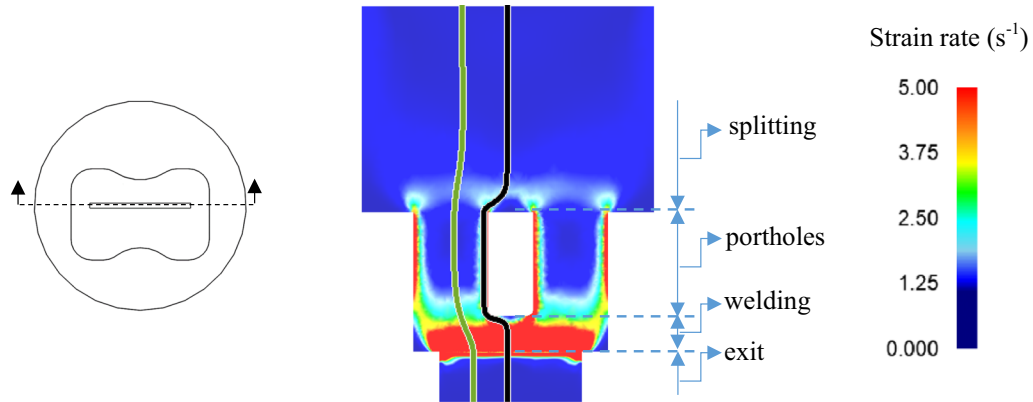


Fig. 17—FEM model predictions for effective strain rate distribution for the section shown on the left.

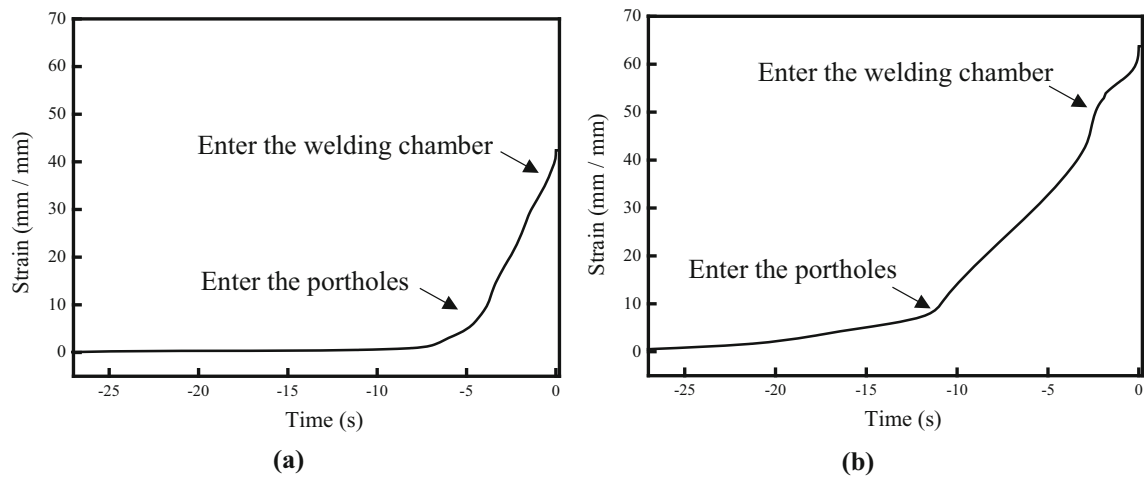


Fig. 18—FEM model predictions for the von Mises equivalent strain history for a streamline which exits at the center of the strip as a function of time for (a) die with streamlined bridge and (b) die with flat bridge.

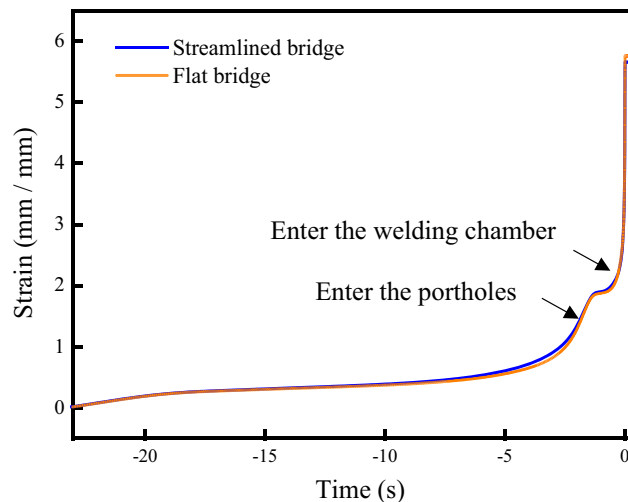


Fig. 19—FEM model predictions for the von Mises equivalent strain history for the extruded strip quarter width point during porthole extrusion as a function of time, for both bridge geometries.

texture at these locations was consistent with a plane strain deformation texture produced at high temperatures.

ACKNOWLEDGMENTS

This work was undertaken, in part, thanks to funding from the Canada Research Chair program (Poole). Additional support was provided by Rio Tinto Aluminum, the Ford Motor Company, and NSERC Canada.

REFERENCES

1. B. Lynn and J. Joe, Aluminum Extrusion Aids Auto Lightweighting. (Design News, 2015), https://cdn.ymaws.com/sites/aec.site-ym.com/resource/resmgr/PDFs/AlExtAidsAutoLtwng_DN115289.pdf, Accessed 23 Sept 2020.
2. Y. Abe, T. Kato, and K. Mori: *J. Mater. Process. Technol.*, 2009, vol. 209, pp. 3914–22.

3. S. Kaya: *Int. J. Adv. Manuf. Technol.*, 2014, vol. 77, pp. 807–17.
4. J. Yu, G. Zhao, and L. Chen: *J. Mater. Process. Technol.*, 2016, vol. 230, pp. 153–66.
5. Y.A. Khan, H.S. Valberg, and B.O.T. Jacobsen: *Int. J. Mater. Form.*, 2010, vol. 3, pp. 379–82.
6. F. Gagliardi, M. Schwane, T. Citrea, M. Haase, N.B. Khalifa, and A.E. Tekkaya: *Key Eng. Mater.*, 2014, vols. 622–623, pp. 87–94.
7. F. Gagliardi, I. Alfaro, G. Ambrogio, L. Filice, and E. Cueto: *J. Mech. Sci. Technol.*, 2013, vol. 27, pp. 1089–95.
8. F. Gagliardi, G. Ambrogio, and L. Filice: *Cirp Ann-Manuf. Technol.*, 2012, vol. 61, pp. 231–34.
9. D. Tang, W. Fang, X. Fan, T. Zou, Z. Li, H. Wang, D. Li, Y. Peng, and P. Wu: *Materials*, 2018, vol. 12, p. 16.
10. J. Yu, G. Zhao, C. Zhang, and L. Chen: *Mater. Sci. Eng. A*, 2017, vol. 682, pp. 679–90.
11. G.J. Chen, L. Chen, G.Q. Zhao, C.S. Zhang, and W.C. Cui: *J. Alloys Compd.*, 2017, vol. 710, pp. 80–91.
12. K. Zhang, K. Marthinsen, B. Holmedal, T. Aukrust, and A. Segatori: *Mater. Sci. Eng. A*, 2018, vol. 722, pp. 20–29.
13. L. Chen, G. Chen, J. Tang, G. Zhao, and C. Zhang: *Mater. Charact.*, 2019, vol. 158, p. 109953.
14. D. Tang, X.H. Fan, W.L. Fang, D.Y. Li, Y.H. Peng, and H.M. Wang: *Mater. Charact.*, 2018, vol. 142, pp. 449–57.
15. X. Xu, G. Zhao, Y. Wang, X. Chen, and C. Zhang: *Vacuum*, 2019, vol. 167, pp. 28–39.
16. C.L. Liu, X. Wang, N.C. Parson, and W.J. Poole: *Mater. Sci. Eng. A*, 2020, p. 140605.
17. W. Fang, D. Tang, H. Wang, D. Li, and Y. Peng: *J. Mater. Process. Technol.*, 2020, vol. 277, p. 116418.
18. C. Zhang, G. Zhao, Z. Chen, H. Chen, and F. Kou: *Mater. Sci. Eng. B*, 2012, vol. 177, pp. 1691–97.
19. M. Schikorra, L. Donati, L. Tomesani, and A.E. Tekkaya: *J. Mater. Process. Technol.*, 2008, vol. 201, pp. 156–62.
20. C.S. Zhang, G.Q. Zhao, Y.J. Guan, A.J. Gao, L.J. Wang, and P. Li: *Int. J. Adv. Manuf. Technol.*, 2015, vol. 78, pp. 927–37.
21. M. Schikorra, L. Donati, L. Tomesani, and A.E. Tekkaya: *J. Mech. Sci. Technol.*, 2007, vol. 21, pp. 1445–51.
22. C. Jowett, Y. Mahmoodkhani, N.C. Parson, and G. Garza: *Proceedings of Eleventh International Aluminum Extrusion Technology Seminar and Exposition*, 2016, Chicago.
23. X. Duan and T. Sheppard: *Metall. Mater. Trans. A*, 2003, vol. 351A, pp. 282–92.
24. C.M. Sellars and W.J. McTegart: *Acta Metall.*, 1966, vol. 14, pp. 1136–38.
25. X. Qian, N. Parson, and X.G. Chen: *Mater. Sci. Eng. A*, 2019, vol. 764, p. 138253.
26. C. Sellars and W.M. Tegart: *Int. Metall. Rev.*, 1972, vol. 17, pp. 1–24.
27. T. Sheppard and D. Wright: *Met. Technol.*, 1979, vol. 6, pp. 215–23.
28. S.M. Lou, Y.X. Wang, C.X. Liu, S. Lu, S.J. Liu, and C.J. Su: *J. Mater. Eng. Perform.*, 2017, vol. 26, pp. 4121–30.
29. C. Zhang, M. Wen, G. Zhao, L. Chen, W. Sun, and K. Bai: *Thin Wall Struct.*, 2019, vol. 135, pp. 65–77.
30. T. Sheppard and A. Jackson: *Mater. Sci. Technol.*, 1997, vol. 13, pp. 203–09.
31. Y. Liu, C. Geng, Q. Lin, Y. Xiao, J. Xu, and W. Kang: *J. Alloys Compd.*, 2017, vol. 713, pp. 212–21.
32. Y. Mahmoodkhani, J. Chen, M.A. Wells, W.J. Poole, and N.C. Parson: *Metall. Mater. Trans. A*, 2019, vol. 50A, pp. 5324–35.
33. Y. Mahmoodkhani, M.A. Wells, N. Parson, and W.J. Poole: *J. Mater. Process. Technol.*, 2014, vol. 214, pp. 688–700.
34. N. Nanninga, C. White, O. Mills, and J. Lukowski: *Int. J. Fatigue*, 2010, vol. 32, pp. 238–46.
35. A.J. den Bakker, X. Wu, L. Katgerman, and S. van der Zwaag: *Mater. Sci. Technol.*, 2015, vol. 31, pp. 94–104.
36. X.H. Fan, D. Tang, W.L. Fang, D.Y. Li, and Y.H. Peng: *Mater. Charact.*, 2016, vol. 118, pp. 468–80.
37. Z.J. Wang, L. Zhai, M. Ma, H. Yuan, and W.C. Liu: *Mater. Sci. Eng. A*, 2015, vol. 644, pp. 194–203.
38. G. Liu, J. Zhou, and J. Duszczuk: *J. Mater. Process. Technol.*, 2008, vol. 200, pp. 185–98.

Publisher's Note Springer Nature remains neutral with regard to jurisdictional claims in published maps and institutional affiliations.